QUARTERLY JOURNAL OF THE ROYAL METEOROLOGICAL SOCIETY
Q. J. R. Meteorol. Soc. **133**: 765–780 (2007)
Published online in Wiley InterScience
(www.interscience.wiley.com) DOI: 10.1002/qj.53

Reproducing cloud microphysical and irradiance measurements using three 3D cloud generators

K. Sebastian Schmidt[a]* , Victor Venema[b], Francesca Di Giuseppe[c], Ronald Scheirer[d,e], Manfred Wendisch[f] and Peter Pilewskie[a]

[a] *Laboratory for Atmospheric and Space Physics, University of Colorado, USA*
[b] *Meteorologisches Institut der Universität Bonn, Germany*
[c] *Agenzia Regionale Prevenzione Ambientale – Servizio IdroMeteorologico Bologna, Italy*
[d] *Sveriges Meteorologiska och Hydrologiska Institut, Sweden*
[e] *Institut für Physik der Atmosphäre, Deutsches Zentrum für Luft- und Raumfahrt, Germany*
[f] *Institut für Physik der Atmosphäre, Universität Mainz, Germany*

ABSTRACT: Using three cloud generators, three-dimensional (3D) cloud fields are reproduced from microphysical cloud data measured *in situ* by aircraft. The generated cloud fields are used as input to a 3D radiative transfer model to calculate the corresponding fields of downward and upward irradiance, which are then compared with airborne and ground-based radiation measurements. One overcast stratocumulus scene and one broken cumulus scene were selected from the European INSPECTRO field experiment, which was held in Norwich, UK, in September 2002. With these data, the characteristics of the three different cloud reproduction techniques are assessed. Besides vertical profiles and histograms of measured and modelled liquid water content and irradiance, the horizontal structure of these quantities is examined in terms of power spectra and autocorrelation lengths. 3D radiative transfer calculations are compared with the independent pixel approximation, and their differences with respect to domain-averaged quantities and 3D fields are interpreted. Copyright © 2007 Royal Meteorological Society

KEY WORDS 3D radiative transfer; cloud model; cloud variability

Received 2 August 2006; Revised 9 February 2007; Accepted 13 February 2007

1. Introduction

Three-dimensional (3D) cloud geometrical and optical variability extends over a wide range of spatial scales. It is often neglected in fields such as remote sensing or energy budget calculations, where one-dimensional (1D) approximations are applied for the solution of the radiative transfer equation (RTE). To separate sources of short-wave radiative biases produced by unresolved cloud variability, three methods for solving the RTE are commonly used, in which the dimensionality is progressively reduced: full 3D calculation; the independent pixel approximation (IPA); and the plane parallel (PP) method (e.g. Cahalan *et al*., 1994; Di Giuseppe and Tompkins, 2003). The difference between the IPA and PP calculations allows one to evaluate the effects of cloud heterogeneity due to the nonlinear relationship between cloud optical thickness and albedo (PP bias). The 3D–IPA contrast quantifies the effect of neglecting horizontal photon transport between independent 1D columns (IPA bias), which is related to the geometrical structure of the cloud field. From analysis of these two different biases it is possible to quantify how the mean radiative properties of the atmosphere are affected by the cloud horizontal heterogeneity and horizontal photon transport.

Such 3D–1D errors represent an accurate estimate of the true error only if the input cloud field provides a realistic representation of the cloud structure. Unfortunately, it is a challenge in itself to find sources for 3D cloud fields that are computationally inexpensive, physically consistent, and tied to actual measurements. Input to the radiative calculations can be provided by idealized, physical, or statistical cloud models, with different levels of incorporation of remote-sensing or *in situ* cloud data. Idealized cloud models allow one to conduct systematic sensitivity studies (e.g. Davies, 1978; Welch and Wielicki, 1984; Kite, 1987) with a variety of cloud types and shapes, solar zenith angles, and optical properties. More realistic clouds are generated with statistical (stochastic) cloud models, in which scale invariance and symmetries (Lovejoy and Schertzer, 1986) are used to extrapolate 3D cloud fields from lower-dimensional measurements (aircraft, radar, satellite). The bounded-cascade model of Cahalan *et al*. (1994), for example, implicitly uses the Kolmogorov eddy dissipation law by adopting a log–log power spectrum of the liquid water cloud in the horizontal. It is usually applied to stratocumulus regimes in overcast conditions (Davis *et al*., 1997; Marshak *et al*.,

* Correspondence to: K. Sebastian Schmidt, University of Colorado, Laboratory for Atmospheric and Space Physics, Campus Box 392, Boulder, CO 80309-0311, USA.
E-mail: sebastian.schmidt@lasp.colorado.edu

1998). Today's statistical cloud generators enable an accurate representation of cloud measurements from different platforms, not only in the horizontal but in all three dimensions (Evans and Wiscombe, 2004; Venema *et al.*, 2006). In other approaches, cloud fields are generated from aircraft measurements (Los and Duynkerke, 2000) or remote-sensing data (Benner and Evans, 2001) by mapping observations directly onto a model grid where information about missing dimensions, such as vertical structure, is filled in using certain assumptions (such as adiabatic vertical profile). Physical models – that is, cloud-resolving models (CRMs) or large eddy simulations (LESs) are based on cloud dynamics and thus have the advantage of being physically consistent (Moeng *et al.*, 1996). LES models have been successfully used to reproduce aircraft cloud microphysical measurements (Neggers *et al.*, 2003). However, they are computationally expensive, and require specification of atmospheric and surface parameters with high accuracy and spatial resolution.

In this study, three new cloud generators are examined. The three different methods reproduce airborne microphysical measurements in a statistical sense. They are applied to a stratiform cloud situation and a convective-boundary-layer cloud situation. The structure of the 3D cloud fields produced is validated with the microphysical measurements. Subsequently, the 3D irradiance fields from radiative transfer calculations are compared with ground-based and airborne measurements. From comparison of the modelled microphysical and radiative fields with their measured counterparts, we try to address the following specific questions:

- How well are microphysical cloud properties reproduced by the three cloud generators (vertical profiles, cloud cover, horizontal structure)?
- How do measured and 3D-modelled solar spectral irradiance compare (domain-averaged and horizontal fields)?
- How sensitive are the modelled irradiance fields and the domain-averaged quantities to differences in the structure of the input cloud fields?
- Under what circumstances do we need a full 3D treatment rather than the computationally much faster IPA?
- Are the 3D effects dependent on wavelength?

In Section 2, the instruments and data are described. The radiative transfer model (Section 3) and the three cloud generators (Section 4) are then introduced. In Section 5, the irradiance fields and the domain-averaged quantities are compared for the two cases studied. Conclusions are presented in Section 6.

2. Instruments and data

The data were collected on 14 and 22 September 2002, during the first field experiment of the INSPECTRO experiment (Kylling *et al.*, 2005), which was conducted on the coast of East Anglia, UK. Data collected by a Partenavia aircraft (Enviscope GmbH, Germany), as well as from one of the ground stations, were used.

2.1. Instruments

The cloud drop size distribution was measured with a Fast Forward Scattering Spectrometer Probe (Fast-FSSP) (Brenguier *et al.*, 1998). From these measurements, the effective radius R_{eff} was derived with an accuracy better than 5%. The liquid water content (LWC) was measured with a Particle Volume Monitor (PVM-100A) (Gerber *et al.*, 1994), with an accuracy better than 5% for cloud drop diameters below 20 μm (Wendisch *et al.*, 2002). On the same aircraft, an albedometer (Wendisch *et al.*, 2001) was mounted, including two horizontally-stabilized optical inlets for measuring the upward and downward spectral irradiance from 290–1000 nm wavelengths, with a spectral resolution of 2–3 nm and an accuracy of 5%. The horizontal stabilization is necessary to avoid problems related to changes in the aircraft attitude. At the ground, a spectrometer with a wavelength range of 500–950 nm was used.

2.2. Data

Figure 1 shows two photographs of the cloud scenes investigated here, as seen from the aircraft. On 14 September 2002, a stratocumulus layer was observed at an altitude of between 550 m and 1000 m. Six vertical profiles were flown, as well as three horizontal flight legs above, and one within the cloud layer. The measurements of 22 September 2002 represent a case of broken cloud. Most of the clouds were encountered at altitudes between 900 m and 1100 m; the cloud cover measured within this altitude range was about 35%. (The cloud cover in a layer is obtained by dividing the number of data points within one height layer for which LWC is above a threshold value (e.g. 0.05 g m^{-3}) by the total number of data points in the layer.) There was no uniform distribution of the clouds throughout the sampled area. The measured cloud cover, as well as cloud base and top height, is dependent on the chosen flight track and might not be representative of the actual situation; and the varying microphysical and geometrical properties are not necessarily captured by the aircraft.

On both days, the clouds were non-precipitating, with drop diameters less than 20 μm. No cirrus was observed. The triangular flight patterns were mostly over land. Only the data over land were used for this study.

Because of the diurnal pattern in the downward irradiance $F^{\downarrow}$, the irradiance measurements for 14 September were rescaled to the solar zenith angle ($SZA = 55^{\circ}$) at 0955 UTC:

$$F_{\cos} = F\frac{\cos(55^{\circ})}{\cos(SZA)}. \tag{1}$$

For the whole flight (0955–1240 UTC), the solar zenith angle ranged from 55° to 50°. Likewise for 22

DOI: 10.1002/qj

Figure 1. Photographs of cloud fields taken from aircraft. Left: stratocumulus on 14 September 2002 (overcast). Right: cumulus on 22 September 2002 (broken cloud).

September, measurements were rescaled to $SZA = 59°$ (flight period 1220–1450 UTC, corresponding to solar zenith angles from 53° to 65°). With this correction, the downward irradiance above the cloud is nearly constant throughout the flights. Strictly, this correction is only valid for the direct (downward) component. Here, it is applied to the upward component $F^{\uparrow}$ as well, because to first order, the upward irradiance will change by about the same amount as the incident downward irradiance. However, scattering might account for a certain amount of overcorrection, not only for the upward but even for the downward component (Schmidt, 2005).

3. Radiative transfer calculations

For the 3D radiative transfer calculations, a Monte Carlo (MC) model for the physically correct tracing of photons in cloudy atmospheres, MYSTIC (Mayer, 1999) was used. This model was validated in an intercomparison of 3D radiation codes (Mayer, 2000). It is a forward photon tracing method that is embedded within the freely available LibRadtran model package (Mayer and Kylling, 2005).

Calculations were performed for wavelengths of 481, 500, 565, 670, 865 and 936 nanometres. The 1D input of MYSTIC comprises profiles of air pressure, temperature, density, and water vapour amount, from the aircraft measurements, complemented by radio soundings (Nottingham) for altitudes above the maximum flight altitude and by the midlatitude summer standard atmosphere (Anderson *et al.*, 1986). The atmosphere was subdivided into 92 layers, with 50 m vertical resolution from ground to 3 km, and resolutions from 1 km to 5 km at altitudes from 3 km to 120 km. The cloud LWC and R_{eff} are the only variable 3D model inputs. The 35 × 35 km model box is subdivided into 350 × 350 pixels; the vertical structure is the same as in the atmospheric profile. Thus each grid box has dimensions of 100 × 100 × 50 m. From the given LWC and R_{eff} at each grid box, cloud drop extinction, single-scattering albedo and phase function are obtained from look-up tables. These are generated by Mie calculations for the required wavelength range, using code by Wiscombe (1980). R_{eff} is used to pick a phase function and single-scattering albedo.

The aerosol optical thickness at 632 nm was monitored by the vehicle-mounted LIDAR system VELIS (Gobbi *et al.*, 2004) at one of the ground stations near the coast. For 14 September, an aerosol optical thickness of 0.05 was reported; for 22 September, it was 0.04 most of the time and reached 0.11 at the end of the flight. Under cloud-free conditions, the low (0.04) and moderate (0.11) aerosol load correspond to a maximal increase of upward irradiance by $12\,\mathrm{mW\,m^{-2}\,nm^{-1}}$ and $30\,\mathrm{mW\,m^{-2}\,nm^{-1}}$ respectively. In cloud-covered areas, the combined aerosol and cloud optical thickness was not considerably larger than the cloud optical thickness alone. Therefore, aerosols were neglected in this study.

The spectral surface albedo was taken from Bowker *et al.* (1985) for grass. It was assumed constant throughout the model box. Although the measurement region contains mainly pasture land, and no sea or large settlements, there might be some contribution from surface variability that is not accounted for by the model.

The number of photons was chosen so that the statistical error of the upward irradiance above cloud top at the individual grid points is below 3%. For each wavelength, 5×10^8 photons were used. As solar spectral input, the 1 nm-resolution version of the Kurucz (1992) data was used. Periodic boundary conditions were applied.

4. Cloud generators

The challenge for 3D radiative transfer simulations based on actual cloud observations is to produce a 3D cloud field (in the present case with a volume of about 500 km^3) from sparse information along a 1D flight track with only a few litres of cloud volume sampled by a microphysics probe (Evans *et al.*, 2003). There are several ways to extrapolate from the lower-dimensional data to the full 3D cloud field, requiring various physical or statistical assumptions.

In contrast to CRM or LES, where the cloud fields produced are not necessarily compliant with microphysical measurements, the three cloud generators used in

DOI: 10.1002/qj

this paper, described below, are aimed at maximizing the weight of observations for cloud reproductions:

- Cloud liquid water content and effective radius retrieval by automated use of aircraft measurements (CLABAUTAIR) (Scheirer and Schmidt, 2005);
- An iterative amplitude-adjusted Fourier transform algorithm (IAAFT) (Venema *et al.*, 2006);
- A spectral idealized thermodynamically-consistent model (SITCOM) (Di Giuseppe and Tompkins, 2003).

4.1. CLABAUTAIR

The CLABAUTAIR algorithm maps aircraft measurements directly onto a model grid. It depends upon schemes used by Los and Duynkerke (2000) and Räisänen (2003) in which aircraft measurements along a flight leg are assumed to be representative across flight direction as well, and some additional assumptions are used for the vertical. For CLABAUTAIR, multiple flight legs in various directions are used, and the gaps without measurements are filled by using the autocorrelation functions along different directions.

In short, the algorithm performs the following steps:

- Identify the main in-cloud flight directions and calculate autocorrelation functions $c_n(\Delta x)$ along N legs (directions).
- Subtract the layer mean from the LWC measurements, and map these onto the grid x_{ij}.
- To fill an empty box at x (where no measurements are available), apply the formula

$$l(x) = \frac{\sum_{n=1}^{N} \sum_{i,j} c_n(|x - x_{ij}|) l(x_{ij})}{\sum_{n=1}^{N} \sum_{i,j} c_n(|x - x_{ij}|)}, \qquad (2)$$

  where x_{ij} denotes the already-filled boxes, and $l = LWC - \overline{LWC}$. The first sum in the numerator runs over all N flight directions; the second over the already-filled boxes x_{ij} along direction n departing from the empty pixel x. (The calculation of $l(x)$ is postponed if there are not enough filled neighbour boxes. If boxes above or below x are filled, they are also considered in Equation (2), with $c_n = 0.95$.)
- Iterate until a value of $l(x)$ has been assigned to all grid points.
- For each layer h, generate a vector (of length equal to the number of boxes per layer) of LWC values that exactly fit the measured probability density function (PDF) $p(LWC, h)$ at altitude h. Cloud-free parts are represented by zero values. Sort the LWC vector and $l(x)$, and map the largest values of LWC onto the largest values of $l(x)$.

For R_{eff}, the same approach is used. Since the independent treatment of both fields may not be physically realistic, the largest values of R_{eff} are assigned to the boxes with largest LWC, according to the measured PDF, separately for each level.

This algorithm is fast and easy to use. For orographic clouds, cloud streets, or any other pattern with locally bounded cloud accumulation, CLABAUTAIR is able to reproduce the pattern without resorting to Fourier space. Simulating flight tracks through CRM clouds, Scheirer and Schmidt (2005) show that with more flight directions available, the reproduced cloud fields are in closer agreement with the original cloud field.

CLABAUTAIR can be obtained from http://www.smhi.se/cloud_generator/.

4.2. IAAFT

The IAAFT algorithm generates so-called surrogate cloud fields based on an LWC distribution and its power spectrum (Venema *et al.*, 2006). It can generate a field with exactly the measured LWC values and almost the exact spatial autocorrelations. To this end, the iterative algorithm repeatedly applies two steps to the surrogate field. First, complex Fourier coefficients ($re^{i\phi}$) are computed by combining the Fourier phases (ϕ) obtained from the last iteration with the magnitudes (r) of the Fourier coefficients of the measurement. Using an inverse Fourier transform, these Fourier coefficients are converted back to a time series. Then, the distribution thus obtained is adjusted so that it fits the measured PDF. For example, the highest value of the reproduced field is given the highest measured value. As this changes the Fourier spectrum, both steps are repeated until both the reproduced PDF and the power spectrum agree with the measurements. As the power spectrum is equivalent to the autocorrelation function, this means that the spatial correlations closely match those of the measurement.

It is also possible to include directly measured constraints by inserting an additional step between adjustment of the power spectrum and adjustment of the PDF. For the overcast case, the gridded *in situ* measured LWC values are forced on the surrogate field. As these data are so sparse, they do not have a significant influence on the cloud field in this case. Cases with more data show that the positions of the clouds (or of their minima and maxima) can be moved to the right positions (Venema *et al.*, 2006). Other possible measured constraints, not used in this study, include a 2D LWP field and a 2D cloud mask or cloud fraction field. These fields can be prescribed at the same resolution as the surrogate field or at a coarser resolution. In this way, the IAAFT algorithm is able to integrate measurements from multiple sources – for example, from radar or microwave-radiometer 2D scans.

To calculate the power spectrum, we use the horizontal flight legs, which are binned into 100 m segments. Because little information on the horizontal spatial correlations, and almost no information on the vertical correlations, is available from an *in situ* measurement, we assume that the correlations are the same in all directions.

DOI: 10.1002/qj

That is, we calculate a 3D isotropic power spectrum from a 1D spectrum.

Before applying the IAAFT algorithm, we subtract the mean LWC profile; we add it again afterwards. The total variance of the 3D power spectrum is adjusted to fit the variance of the zero-mean LWC distribution. The R_{eff} field of the IAAFT clouds is derived by keeping the measured pairs of LWC and R_{eff} together. In other words, the R_{eff} values are perturbed and distributed in the same way as the LWC values.

IAAFT can be obtained from http://www.meteo.uni-bonn.de/venema/themes/surrogates/iaaft/.

4.3. SITCOM

The SITCOM cloud generator utilizes a hybrid approach between statistical and physical models. To reconstruct a 3D cloud field, it uses at each height z: the *total* water $q_{\mathrm{t}}(z)$; the layer temperature $T(z)$; and the total water variability $\sigma^2_{q_{\mathrm{t}}}(z)$. The thermodynamical inputs are the profiles of total water and temperature; and the cloud *liquid* water is diagnosed from these quantities assuming that no supersaturation can occur. To obtain $q_{\mathrm{t}}(x, y, z)$, a total water *anomalies* field $q'_t(\nu_x, \nu_y)$ is prescribed for each height z through a power spectrum

$$\mathcal{P}_z(r_\nu) \approx \sigma^2_{q_{\mathrm{t}}}(z) r_\nu{}^{-\beta} \exp\left[-\left(\frac{r_{\nu_0}}{r_\nu}\right)^n\right], \qquad (3)$$

where ν_x and ν_y are frequencies in the x and y directions and

$$r_\nu = \sqrt{\nu_x^2 + \nu_y^2}.$$

This functional choice generates a power-law dependence of $q_{\mathrm{t}}(x, y, z)$ with respect to ν_x and ν_y, and at the same time allows the incorporation of a long-wavelength cut-off through the definition of r_{ν_0} and n. When r_{ν_0} has a value smaller than $1/L$, where L is the domain horizontal dimension, a preferred scale for the total water variability is created, which is more pronounced for higher values of n. The normalization factor $\sigma^2_{q_{\mathrm{t}}}(z)$ represents the power spectrum integral over the whole frequency domain, and is set equal to the variance of $q_t(x, y, z)$ for given height z. The purpose of rescaling by $\sigma^2_{q_{\mathrm{t}}}(z)$ is to ensure consistency between observed and simulated total water variance profiles.

The SITCOM input r_{ν_0}, n and β, as well as $q_{\mathrm{t}}(z)$, $T(z)$ and $\sigma^2_{q_{\mathrm{t}}}(z)$, were derived from aircraft measurements averaged along horizontal legs at the available altitudes within clouds. Since no preferred scale was observed during either flight, a value of $r_{\nu_0} = 1/L$ (with L the box length, 35 km) was used (with $n = 1$); β was found to be 1.28 for the 14 September case and 2.27 for the 22 September case. The cloud *liquid* water at each height, $q_{\mathrm{l}}(x, y, z)$, is diagnosed from the comparison between the total water field $q_{\mathrm{t}}(x, y, z)$ and the saturation mixing ratio $q_{\mathrm{sat}}(z)$ (derived from the temperature profile) by simply assuming no supersaturation, i.e. that

$$q_{\mathrm{l}}(x, y, z) = q_{\mathrm{t}}(x, y, z) - q_{\mathrm{sat}}(z).$$

For the effective radius, the measured mean profile was used throughout the model domain.

The original purpose of SITCOM was to use $q_{\mathrm{t}}(z)$ and $T(z)$ for cloud generation, as needed in climate models. *In situ* cloud probes, however, provide q_{l}. The reproduced cloud fields nevertheless look very realistic (Figure 4). However, the LWC PDFs are not constrained to match the observed ones (Figure 3), as is the case for CLABAUTAIR and IAAFT, which both use the LWC PDF for initialization.

SITCOM can be obtained from http://www.smr.arpa.emr.it/software/sitcom/sitcom.html.

5. Comparison

The validation of the cloud generator output is performed on two levels:

- microphysics – compare the reproduced cloud fields of LWC and R_{eff} with the measurements;
- irradiance – use the cloud fields for 3D radiative transfer calculations and compare the simulated irradiance fields with the measurements.

In both steps, it is impossible to compare the simulated fields directly with measurements, because the simulations represent a snapshot at a fixed time, whereas the measurements are taken at varying space and time points. A direct comparison would only be possible if the cloud structure and the resulting radiation field were measured simultaneously. In the overcast case, the cloud field is assumed to be stationary (moving with the mean wind speed), and the measurements are translated back to a reference time. This correction is not applied in the broken-cloud case, where the lifetime of the clouds is short compared with the measurement period.

For the microphysics step, the data are first filtered so that only the measurements within a 35 × 35 km box (southern limit 52.55 °N, western limit 0.85 °E) entirely over land are used (with wind correction for 14 September, without for 22 September). From these filtered data, 3D fields of LWC and R_{eff} are reproduced. Mean profiles of LWC, R_{eff}, layer cloud fraction, and power spectra along horizontal lines within layers are compared with their measured counterparts. In this way it can be checked how well the generators reproduce domain-averaged microphysical quantities and the horizontal cloud structure.

For the irradiance step, the spectral irradiance of the generated fields is calculated for each grid point for six wavelengths (see Section 3). These model results are evaluated against the measurements by comparing mean profiles, histograms of modelled and measured irradiance at a certain flight level, and power spectra. The histograms are particularly useful in the case of broken cloud, where the mean value at a height level is rather meaningless if the cloud fraction in the generated cloud is not correctly estimated. The histograms allow us to

DOI: 10.1002/qj

Table I. Basic microphysical properties of the reproduced cloud fields.

	CLABAUTAIR	IAAFT	SITCOM
	14 September 2002–overcast		
LWP (g m^{-2})	191	178	157
τ	39	37	35
$\overline{LWC}$ (g m^{-3})	0.39	0.48	0.57
$\overline{R_{\text{eff}}}$ (μm)	7.5	7.2	6.7
	22 September 2002–broken cloud		
LWP (g m^{-2})	3.8	4.9	6.0
τ	1.0	1.1	1.2
$\overline{LWC}$ (g m^{-3})	0.09	0.09	0.10
$\overline{R_{\text{eff}}}$ (μm)	6.4	6.2	7.2

identify modes that can be connected to cloud-free and cloudy regions.

Extending the cloud generator validation from a microphysical comparison to an irradiance comparison also gives insight into how microphysical structure translates into structure of the irradiance field.

5.1. Microphysics

In this step, the output of the three cloud generators is compared with the microphysical measurements. Table I shows mean values of basic properties of the reproduced cloud fields, for the two cloud cases investigated.

The liquid water path (LWP) is the column-integrated LWC. The cloud optical thickness τ relates LWP and R_{eff}:

$$\tau = \frac{3}{2}\frac{LWP}{\rho R_{\text{eff}}}, \tag{4}$$

where ρ is the density of liquid water (Stephens, 1978). The LWC and R_{eff} values are averaged over non-empty cloud boxes only. Although the same microphysical input data are used, there is some variability in the reproduced microphysical parameters for the two cases. The optical thickness τ ranges from 35 to 39 for the overcast case, and from 1.0 to 1.2 for the broken-cloud case. Depending on which definition is used to identify 'cloud' and 'cloud-free' areas, there can be substantial differences in the resulting cloud cover. This is most obvious for the broken-cloud case at altitudes between 1000 m and 1100 m. When using the Fast-FSSP data to determine the cloud cover, a value of 53% is obtained if a non-zero drop concentration is considered a cloud event. In contrast, for the PVM-100A measurements, an LWC offset value is used to distinguish electronic noise from cloud measurements. When using 0.025 g m^{-3} as the offset, a cloud cover of 11% is obtained. Decreasing this threshold gradually increases the resulting cloud cover. If a large portion of cloud contains LWC below the chosen threshold value, this portion is ignored. There is no standard definition of what should be considered 'cloud' in the literature, and all three generators use different definitions (CLABAUTAIR uses a threshold of 0.025 g m^{-3}, IAAFT uses 0.010 g m^{-3}, and SITCOM uses no threshold). Given this variability, it is comforting that the optical thickness is in reasonable agreement for all three generators for both cases. A further difference between the cloud generators is the discretization of the height levels: IAAFT and SITCOM use a 50 m vertical resolution, while CLABAUTAIR uses 100 m. Measurements are very sensitive both to the height level and to the chosen LWC threshold. The highest LWC values for the broken-cloud case are found at altitudes between 1020 m and 1080 m. These fall in two layers for IAAFT (33% reproduced cloud cover at this altitude) and SITCOM (37%), and in one layer for CLABAUTAIR (16%).

The LWC profiles in Figure 2 show more detail than the mean values in Table I. The circles show the PVM measurements, and the lines show the mean LWC profiles of the reproduced cloud fields. For the in-cloud leg at 780 m in the overcast case (Figure 2(a)), the measured LWC is in the range 0.2–0.75 g m^{-3}. Four profiles are available above this height, and one below. While the LWC variability is fully captured on the in-cloud leg, the measurements above and below 780 m do not reflect the full range of LWC. Above 1000 m,

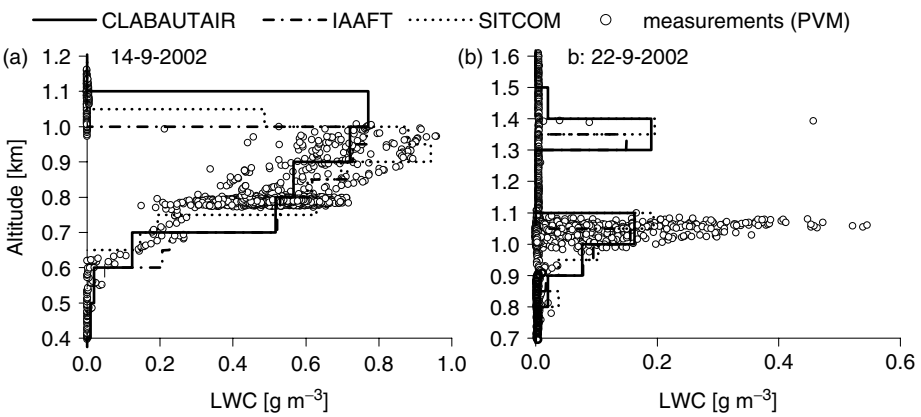

Figure 2. Measured and simulated LWC profiles for (a) the overcast case and (b) the broken-cloud case. The symbols show all aircraft measurements. The lines refer to the mean profiles of the reproduced cloud fields.

DOI: 10.1002/qj

the generators all reproduce a cloud layer, although the measurements do not show any significant LWC above 1020 m. This is because of the discrete height levels of 50 m thickness (IAAFT and SITCOM) or 100 m thickness (CLABAUTAIR). The LWC measured between 1000 m and 1020 m is mapped to a full height level, with a low cloud cover. The same apparent discrepancy is observed in the broken-cloud case (Figure 2(b)), where a cloud layer is reproduced above 1300 m, even though there are very few measurements.

The PDFs in Figure 3 show the distribution of LWC values, within the range 750–800 m for the overcast case, and within the range 1000–1050 m for the broken-cloud case. The bin width is 0.025 g m^{-3}. The dashed lines show the aircraft measurements, the solid lines the reproductions. For 22 September, the value of the PDF at $LWC = 0$ is not shown; it is about 0.9 for the measurements (using the CLABAUTAIR threshold), CLABAUTAIR and SITCOM, and about 0.8 for IAAFT. This difference is caused by the different threshold values used to define the layer cloud fraction. For the overcast case, the reproduced and measured LWC PDFs match for CLABAUTAIR and IAAFT. In this case, the difference between the LWC thresholds has no impact on the result. For the SITCOM cloud, the reproduced variability is larger than observed. A possible reason is that the SITCOM LWC variability is taken from the in-cloud leg, where higher standard deviations prevail. In addition, the mean value of the reproduced SITCOM PDF is slightly above the measurement. For the broken-cloud case, the difference between the reproduced LWC PDFs is larger, probably mainly because of the different LWC threshold values used, and hence different cloud covers. The closest match with the measured PDF is achieved by SITCOM.

Figure 4 shows the horizontal distribution of LWP values in the reproduced clouds for both cases. These pictures allow a qualitative assessment of the cloud structure. The triangular pattern that is seen in both CLABAUTAIR reproductions traces the flight track: in its vicinity, the reproduced variability is higher than in the part of the cloud where no measurements are available. The extent to which the CLABAUTAIR reproductions are representative of the actual cloud structure decreases with the distance of a grid point from an actual measurement. The situation is different for IAAFT and SITCOM, where the reproduced clouds reflect the statistical properties of the measurement no matter where it was taken, and so the cloud structure looks the same all over the measurement grid. In IAAFT, the values along the flight track can optionally be tied to the measurements. This was done for the overcast case. While for IAAFT and SITCOM, the domain size can thus be chosen independently of the area that was actually covered by the aircraft, for CLABAUTAIR the grid must be confined around the flight track. Furthermore, Scheirer and Schmidt (2005) show that the more flight directions are available at different height levels, the better CLABAUTAIR's reproduction of the original cloud. If only one flight leg is available, CLABAUTAIR will produce unphysical results. However, this technique is able to handle gradients in the cloud field if sufficient data are available.

The horizontal scales can be seen quantitatively in Figure 5, which shows power spectra of measured (grey) and reproduced (black) LWC, at an altitude of 780 m for the overcast case and 1050 m for the broken-cloud case. They were obtained by averaging over all east–west lines of the reproduced cloud grid, while the measured values were calculated along the flight track. During this track, the flight direction changed several times. The

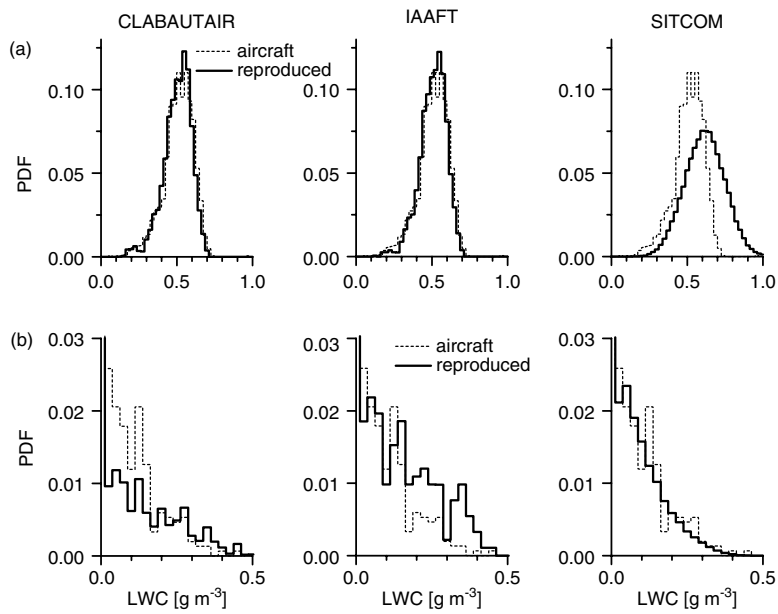

Figure 3. Measured (dashed lines) and simulated (solid lines) LWC PDFs for (a) the overcast case (780 m altitude) and (b) the broken-cloud case (1050 m altitude). For (b), the value of the PDF at LWC = O is above 0.03, see explanations in text.

DOI: 10.1002/qj

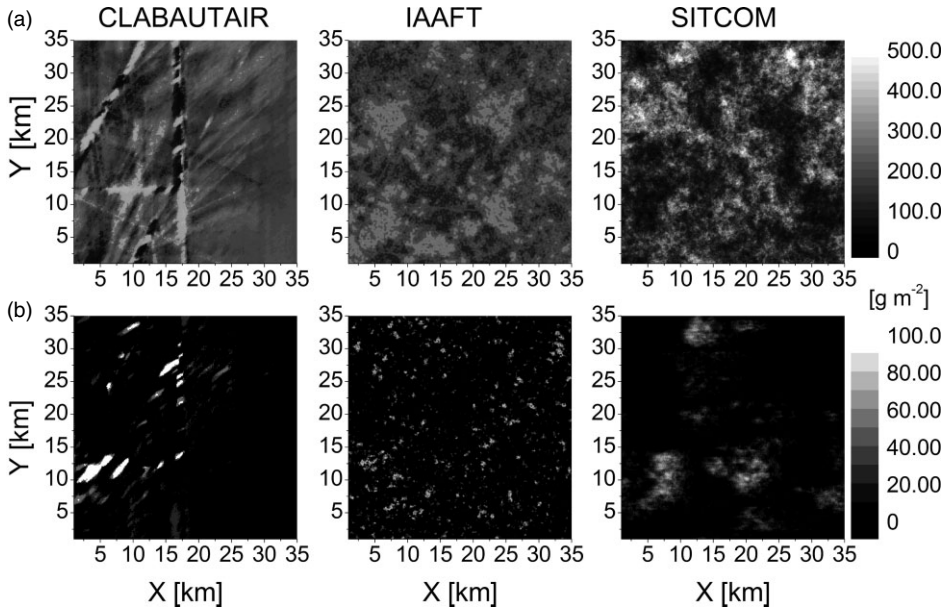

Figure 4. Simulated LWP fields for (a) the overcast case and (b) the broken-cloud case.

power spectra for individual directions (not shown) are similar to the power spectrum representing all flown directions. The grey lines show the measured power spectra, binned in logarithmically equal wave number intervals. For the overcast case, the power spectra of CLABAUTAIR and IAAFT peak at $k \approx 0.2\,\mathrm{km}^{-1}$, which corresponds to 5 km. These 5 km patches are also seen in Figure 4. The level of the power spectra from the broken-cloud case is about one order of magnitude lower at small wave numbers compared with the overcast case. For the overcast case, the autocorrelation length of the measured LWC field (1.3 km) is best reproduced by IAAFT (1.2 km) and SITCOM (1.4 km), and slightly overestimated by CLAUBAUTAIR (1.7 km). The measured autocorrelation length for the broken-cloud case (0.2 km) is only correctly reproduced by IAAFT (0.2 km), and overestimated by SITCOM and CLABAUTAIR (0.6 km).

5.2. Irradiance

5.2.1. Overcast case

For the overcast case, the measured and simulated irradiance spectra are shown in Figure 6. The upper curves show the upward irradiance above the cloud layer, where the measurements have been averaged over a leg flown at 2900 m. The shaded area represents the ± 1 standard deviation range from the measurements. The solid black line shows results from 1D radiative transfer calculations where the mean IAAFT profile of LWC and effective radius are used as input. The symbols show the results of the 3D calculations, averaged over the whole model domain at 2900 m. The results from CLABAUTAIR and IAAFT are very similar. The lower curves show the measured and modelled downward irradiance at the ground. The measurements were made by the ground-based spectrometer with a wavelength range of 500–950 nm; the spectrum is averaged over the flight time. There is very good agreement between all model results and the data. 1D simulations give results similar to those of the 3D calculations. For most wavelengths, both 1D and 3D calculations show slightly higher upward irradiance above clouds (higher reflectance) and lower downward irradiance below clouds (lower transmittance) than measured.

Table II. Domain-averaged irradiance $F^{\uparrow}$ above cloud and $F^{\downarrow}$ below cloud at 500 nm (overcast case). The measurements and simulations above cloud are shown at 1.5 km altitude; below cloud the aircraft measurements were taken in the range 0–400 m, the rest on the ground. For each cloud generator, modelling results are shown for MC calculations (first line), for IPA (second line), and for the 1D equivalent of the reproduced cloud (third line). Modelling results that agree to within $12\,\mathrm{mW\,m^{-2}\,nm^{-1}}$ with the aircraft measurements are marked by asterisks. Mean values are shown, along with standard deviations after the $\pm$ sign.

	$F^{\uparrow}$ above cloud ($\mathrm{mW\,m^{-2}\,nm^{-1}}$)	$F^{\downarrow}$ below cloud ($\mathrm{mW\,m^{-2}\,nm^{-1}}$)
Measurement	844 ± 40	195 ± 30
... on ground		225 ± 108
CLABAUTAIR	861 ± 44	*196 ± 36*
... IPA	863 ± 56	194 ± 52
... 1D	884	173
IAAFT	*855 ± 34*	*201 ± 28*
... IPA	*856 ± 44*	*200 ± 39*
... 1D	866	*186*
SITCOM	828 ± 63	227 ± 55
... IPA	829 ± 82	226 ± 77
... 1D	875	182

DOI: 10.1002/qj

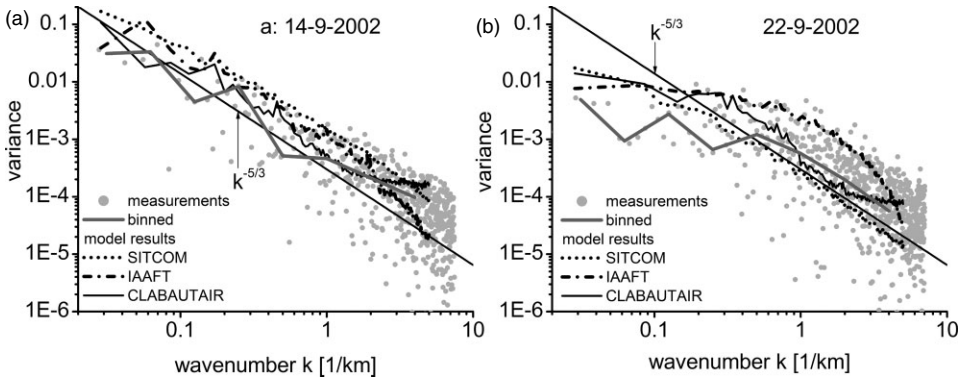

Figure 5. Power spectra (in units of $(\mathrm{g\ m^{-3}})^2$km) of the measured (grey) and simulated (black) LWC fields for (a) the overcast case, at 780 m altitude, and (b) the broken-cloud case, at 1050 m altitude. The simulated power spectra were calculated along all east–west lines and averaged, while the measured values were calculated from one horizontal in-cloud leg. The grey lines show the measured power spectra, binned by wave number.

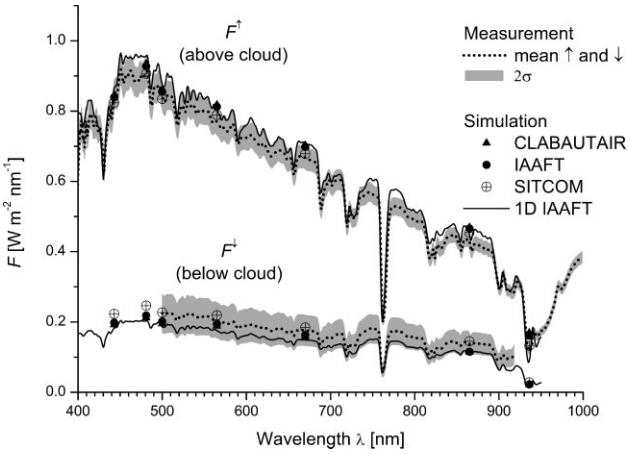

Figure 6. Measured and simulated spectra for the overcast case. Upper curves: $F^{\uparrow}$ above the cloud layer (2900 m). Lower curves: $F^{\downarrow}$ below the cloud layer (ground). The measurements above cloud are averaged over an entire leg. The grey shaded area represents the ± 1 standard deviation range from the measurements. The black dotted lines show the mean measured irradiance. The symbols indicate the mean values of the irradiance simulated by 3D RTM. The black lines show the results obtained from using the mean IAAFT vertical profile as input to a 1D RTM.

Table II compares mean values and standard deviations (shown after the $\pm$ sign) of the measurements and model results at 500 nm wavelength above and below cloud. Below cloud, both aircraft measurements in the range 0–400 m and ground measurements are shown. Modelling results that agree to within 12 mW m^{-2} nm^{-1} with the measurements are marked with an asterisk. The IPA results are obtained by switching off horizontal photon transport in MYSTIC. For the 1D calculations, the 3D clouds are horizontally averaged layer by layer. The closest agreement with the measurements is achieved by IAAFT. The 3D and IPA results are very close for all calculations; hence a full 3D calculation is unnecessary in this case for the domain-averaged irradiances. This accords with previous studies (e.g. Di Giuseppe and Tompkins, 2003). The 1D results are offset by 10–20 mW m^{-2} nm^{-1} from the 3D and IPA results, and from the SITCOM results even by 50 mW m^{-2} nm^{-1}. Both the mean and the standard deviation of the downward irradiance measured by the ground-based spectrometer are higher than those measured by aircraft. By splitting up the ground measurements hour by hour (Schmidt, 2005), one can see that there is a large temporal variability in the irradiance histograms, which cannot be captured by the model simulations.

In Figure 7, the histograms of simulated and measured irradiance at 500 nm for particular height levels are plotted. The upper three panels show the measurements (grey) and simulations (black) of the upward irradiance above the cloud field (1.5 km). The lower panels show the downward irradiance at the ground. In accord with the spectra shown in Figure 6 and Table II, the mean values of measured and simulated irradiance agree both above and below the cloud field for all generators (within 20 mW m^{-2} nm^{-1}). The IPA results (dotted lines) are almost the same as for the 3D calculations. The 1D calculations are within the range of variability of the measurements and the 3D calculations.

Figure 8 shows the horizontal structure of the irradiance field just above the cloud ($F^{\uparrow}$, 1.2 km altitude, middle row), further up ($F^{\uparrow}$, 2.9 km altitude, upper row), and below the cloud field ($F^{\downarrow}$, ground, lower row). At the ground and far above the cloud, the structures have been smoothed out. This geometrical smoothing is only obtained with 3D RTM. The IPA results have the same structure regardless of the vertical separation from the cloud layer. The irradiance field just above cloud top resembles the patterns of the LWP fields shown in Figure 4. Vertical irradiance profiles are obtained by averaging the irradiance field horizontally for each layer. For all wavelengths they compare very well with the measurements (not shown).

In Figure 9, the horizontal structure of the radiative fields is analysed by the power spectrum for $F^{\downarrow}$ on the ground. The measured power spectrum was obtained from the 500 nm time series of the ground-based spectrometer. It is in good agreement with the simulations at scales above 1 km. At smaller scales ($k > 1\ \mathrm{km}^{-1}$),

DOI: 10.1002/qj

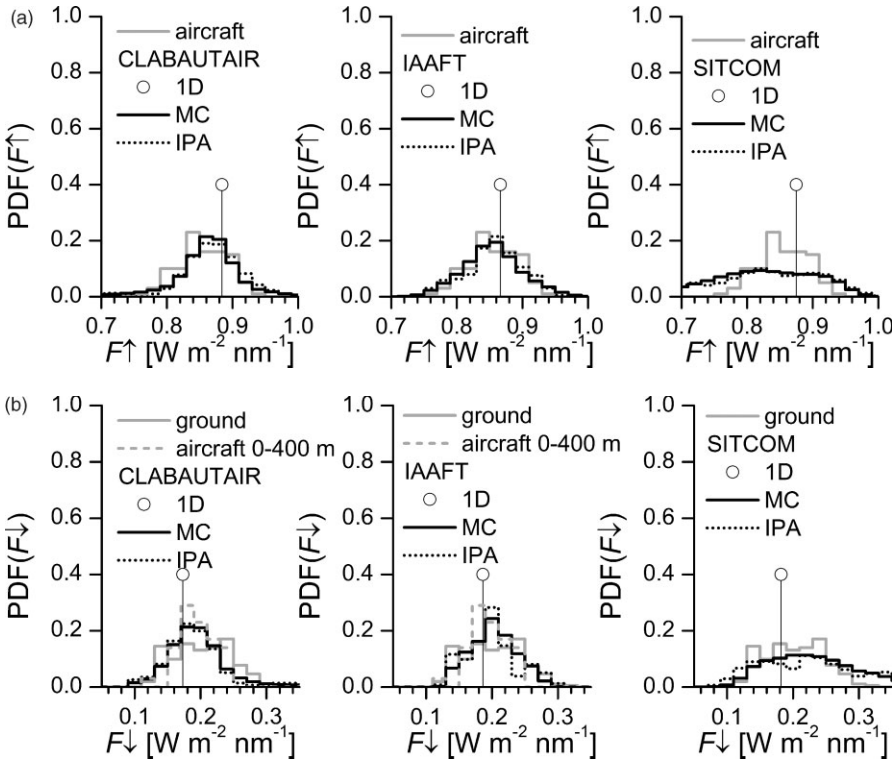

Figure 7. Histograms of measured (grey) and simulated (black) irradiance for the overcast case. (a) Above the cloud layer: $F^{\uparrow}$, 1.5 km. (b) Below the cloud layer: $F^{\downarrow}$, ground measurements (solid grey lines) and aircraft measurements at 0–400 m (dashed grey lines). The dotted black lines show the IPA results; the circles mark the results for the 1D equivalents of the reproduced clouds.

the measured variance is below the noise level of the simulations (10^{-5}) given by the limited photon number. The thin straight line represents the scaling of a $k^{-5/3}$ power law, showing good agreement with measurements and simulations for $k < 0.3\,\mathrm{km}^{-1}$. Above (for small length scales), both measured and simulated variance decrease faster than $k^{-5/3}$: there is less variability on small scales, again because of geometrical smoothing. This irradiance scale break is caused by the geometrical set-up of the scene and by the hemispherical cosine-weighted averaging of the corresponding radiance field. It is, in origin, different from the scale break found by Davis *et al*. (1997) for radiance fields. Other than the radiance scale break, the irradiance scale break changes its position with the distance from the cloud layer. Directly above or below the cloud, the irradiance scale break shifts to small scales. Further away, geometrical smoothing shifts the position of the scale break towards larger scales. For IAAFT, the power spectrum from the IPA calculation is also shown. No scale break is reproduced, because horizontal photon transport is neglected. The first noticeable deviation of the IPA results from the full 3D MC simulations occurs at a scale as large as 10 km. Consequently, in contrast to domain-averaged irradiance, standard IPA calculations are *not* sufficient if the correct structure of the irradiance field for scales smaller than 10 km has to be determined. Hence, while horizontal photon transport is irrelevant to reproducing one-point statistics (mean value, PDF), it becomes important for correctly reproducing two-point statistics (power spectra). The measured correlation length of the 500 nm downward irradiance during the in-cloud leg (0.6 km) is slightly overestimated by CLABAUTAIR (0.9 km) and almost correctly reproduced by IAAFT and SITCOM (0.5 km). Note that the correlation length of the measured LWC (1.3 km) is greater than that observed for the corresponding irradiance (0.6 km).

5.2.2. *Broken-cloud case*

For the broken-cloud case, it is less useful to compare horizontally-averaged irradiance values, because a small difference in the measured or modelled cloud cover changes the mean values substantially. Nevertheless, the measured and simulated downward irradiances below the cloud layer and upward irradiances above the cloud layer are listed in Table III. In this case, no aircraft measurements below cloud were available, and only the ground measurements were used. A standard deviation is only given if the PDF has a single mode. The differences between the modelled and simulated irradiances are 50, 20 and 12 $\mathrm{mW\,m^{-2}\,nm^{-1}}$ ($F^{\uparrow}$) and 45, 15 and 8 $\mathrm{mW\,m^{-2}\,nm^{-1}}$ ($F^{\downarrow}$), for CLABAUTAIR, IAAFT and SITCOM, respectively. Thus, with respect to the mean values, CLABAUTAIR agrees with the measurements to within 50 $\mathrm{mW\,m^{-2}\,nm^{-1}}$, IAAFT to within 20 $\mathrm{mW\,m^{-2}\,nm^{-1}}$, and SITCOM to within 12 $\mathrm{mW\,m^{-2}\,nm^{-1}}$; so SITCOM has the best agreement with the measurements. For IAAFT, two more calculations have been done using MODIS-AQUA satellite data from an overpass at 1245 UTC. For 'C', the reproduced

DOI: 10.1002/qj

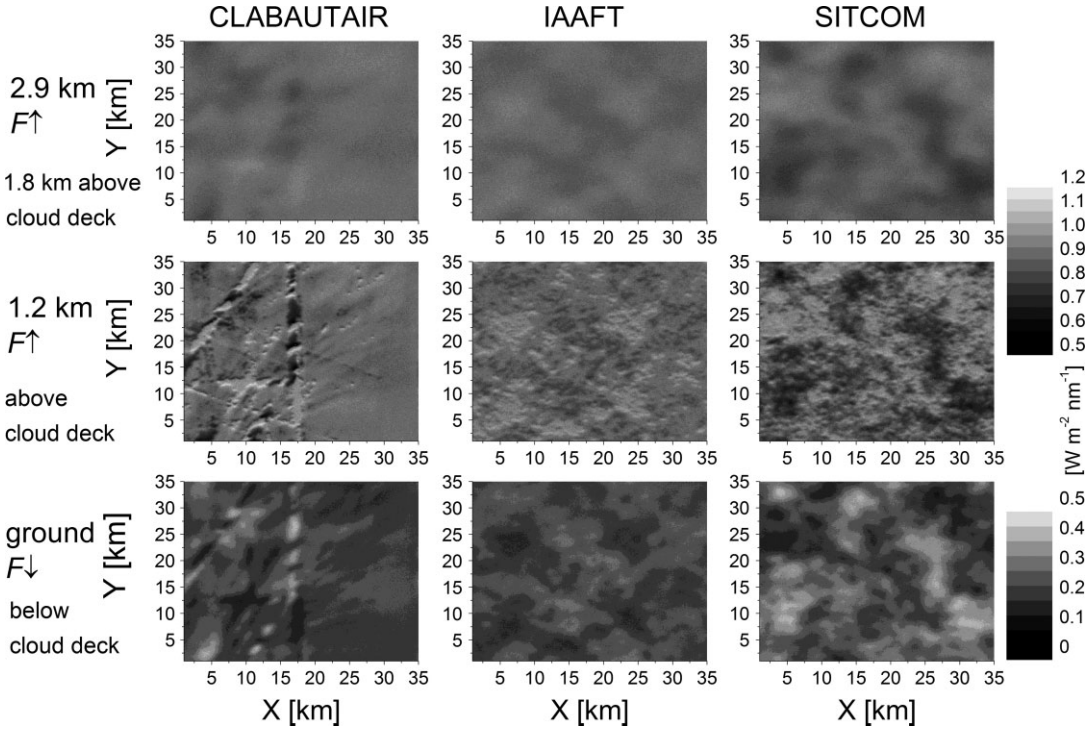

Figure 8. Horizontal distribution of simulated upward irradiance at 2.9 km and 1.2 km altitude, and downward irradiance at the ground (all at 500 nm), for the overcast case.

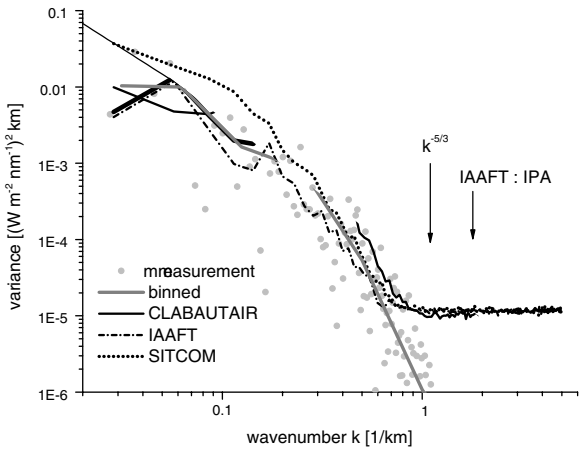

Figure 9. Power spectrum of $F^{\downarrow}$ on the ground (for IAAFT, also including the IPA results), for the overcast case. Measurements are shown by grey symbols and the grey line (logarithmically binned power spectrum); simulations are shown by black lines. For comparison, the $k^{-5/3}$ power law is also shown.

cloud has been forced to have a cloud cover of 63%, as observed by MODIS. This increases the reflected irradiance and decreases the transmitted irradiance beyond the measured values. However, the satellite-retrieved effective drop radius is about three times as high as measured with the Fast-FSSP. Thus a further cloud with both cloud cover and effective radius rescaled to match the satellite observations was generated ('CR'). Only by tuning both cloud cover and effective radius can the modelled irradiance be brought into agreement with the measurements.

Table III. Domain-averaged irradiance $F^{\uparrow}$ above cloud and $F^{\downarrow}$ below cloud at 500 nm (broken-cloud case). The measurements and simulations above cloud are shown at 2.9 km altitude; below cloud, ground measurements are shown. For each cloud generator, modelling results are shown for MC calculations (first line) and IPA (second line). For IAAFT, two more clouds have been produced: by scaling the cloud cover up to what was measured by MODIS (63%) ('C'); and by additionally applying a correction for the effective radius, whose retrieved value was about three times as high as that measured *in situ* ('CR'). Mean values are shown, along with standard deviations after the ± sign in cases where the PDF has a single mode.

	$F^{\uparrow}$ above cloud (mW m^{-2} nm^{-1})	$F^{\downarrow}$ below cloud (mW m^{-2} nm^{-1})
Measurement	175 ± 32	
... on ground		746
CLABAUTAIR	125 ± 46	791
... IPA	122	792
IAAFT	156 ± 20	761
... IPA	149	767
... C	227	695
... CR	167	752
SITCOM	163 ± 70	754
... IPA	169	750

Figure 10 shows the histograms of simulated and measured irradiance at 500 nm above the main cloud layer at 2.9 km (upper row) and below the cloud layer on the ground (lower row). The histogram for the ground measurements (lower row, grey lines) has three maxima.

DOI: 10.1002/qj

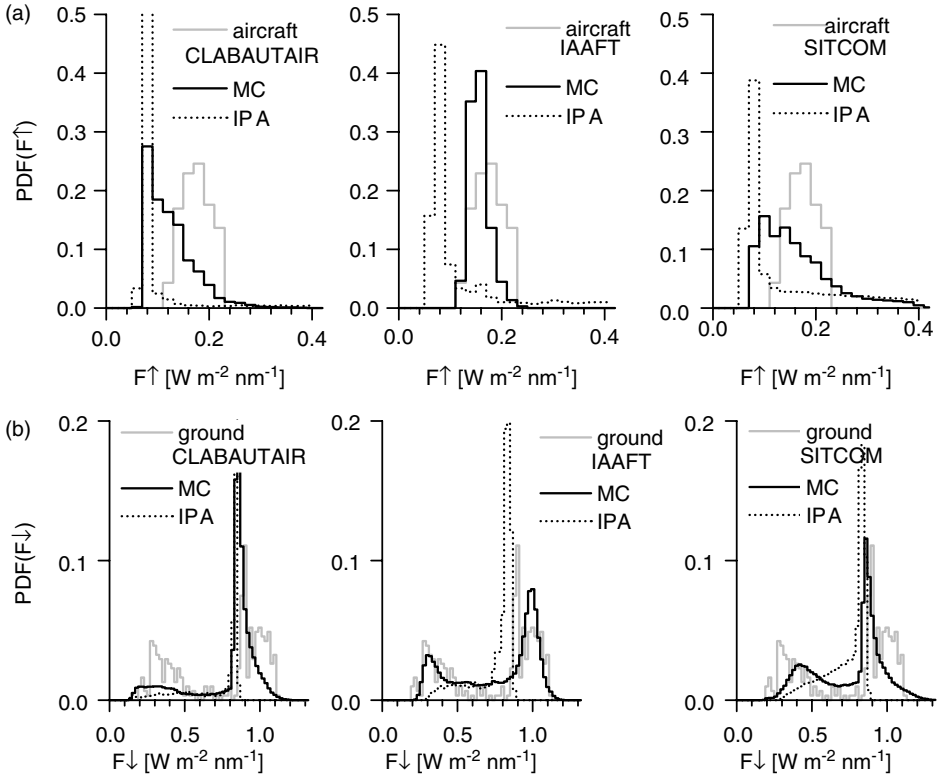

Figure 10. Histograms of measured (grey) and simulated (black) irradiance for the broken-cloud case. Upper row: above the cloud layer ($F^{\uparrow}$, 2.9 km). Lower row: below the cloud layer ($F^{\downarrow}$, ground). The dotted lines show the IPA results.

The modes at 0.3 $\mathrm{Wm^{-2}\,nm^{-1}}$ and 0.8 $\mathrm{Wm^{-2}\,nm^{-1}}$ correspond to measurements under cloudy and clear-sky conditions, respectively. The relative amplitudes of the two peaks reflect the average cloud cover encountered during the measurement period. The integrated area of the modes can be interpreted as the amount of time measured under cloudy and cloudless conditions. A third mode is located above the clear-sky mode, around 1.0 $\mathrm{Wm^{-2}\,nm^{-1}}$. This corresponds to the enhanced irradiance that is encountered in the cloud-free sections between two clouds. The downward irradiance under a 'cloud hole' may be larger than the irradiance measured under cloud-free conditions because of the diffuse radiation originating from scattering at the cloud edges. Although SITCOM matches the measurement best with regard to the mean values, IAAFT is in better agreement with regard to the histogram. However, the clear-sky peak is missing. This is because there were no large cloud-free regions reproduced by IAAFT, and the scattered clouds were evenly distributed over the model domain. The ground-based irradiance measurements, on the other hand, do include periods when no clouds were present. These periods or regions were not captured by the aircraft. As expected, the third mode, originating from cloud edge scattering, is not present in the IPA calculation, where horizontal photon transport is neglected. For SITCOM, the clear-sky peak is overemphasized with respect to the third mode. This is because the cloud parcels reproduced by SITCOM were larger than observed, and cloud gaps were not small enough to correctly model the cloud edge contributions to the total downward irradiance. For CLABAUTAIR the situation is similar; moreover, the amplitude of the cloud peak is underestimated because the overall cloud cover is underestimated by this generator. Therefore the mean value of the downward irradiance at the ground is overestimated with respect to the measurements. This problem will be fixed with the next version of CLABAUTAIR.

For the upward irradiance above the cloud field at 2.9 km altitude (upper row in Figure 10), the IAAFT result is in best agreement with the measurements. For all generators, the peak of the IPA calculation at 0.08 $\mathrm{Wm^{-2}\,nm^{-1}}$ represents reflections by the surface. In the full 3D calculation, this surface mode is not present, thanks to geometrical smoothing. The tail of the distributions as seen in the IPA results stems from grid points with high optical thickness. In the full 3D calculation, the surface mode and the tail recombine through geometrical smoothing. For CLABAUTAIR, the location of the resulting mode is below the measurements. For SITCOM, smoothing has not fully taken effect at 2.9 km altitude; at 5.0 km altitude (not shown), a single mode occurs at about 0.2 $\mathrm{Wm^{-2}\,nm^{-1}}$, in agreement with the measurements.

Figure 11 shows the distribution of irradiance throughout the model domain. Upward and downward irradiance values are plotted at different height levels. As in the overcast case, the field close to the top of the main cloud field is most similar in structure to the microphysical input, while some smoothing is observed at the

DOI: 10.1002/qj

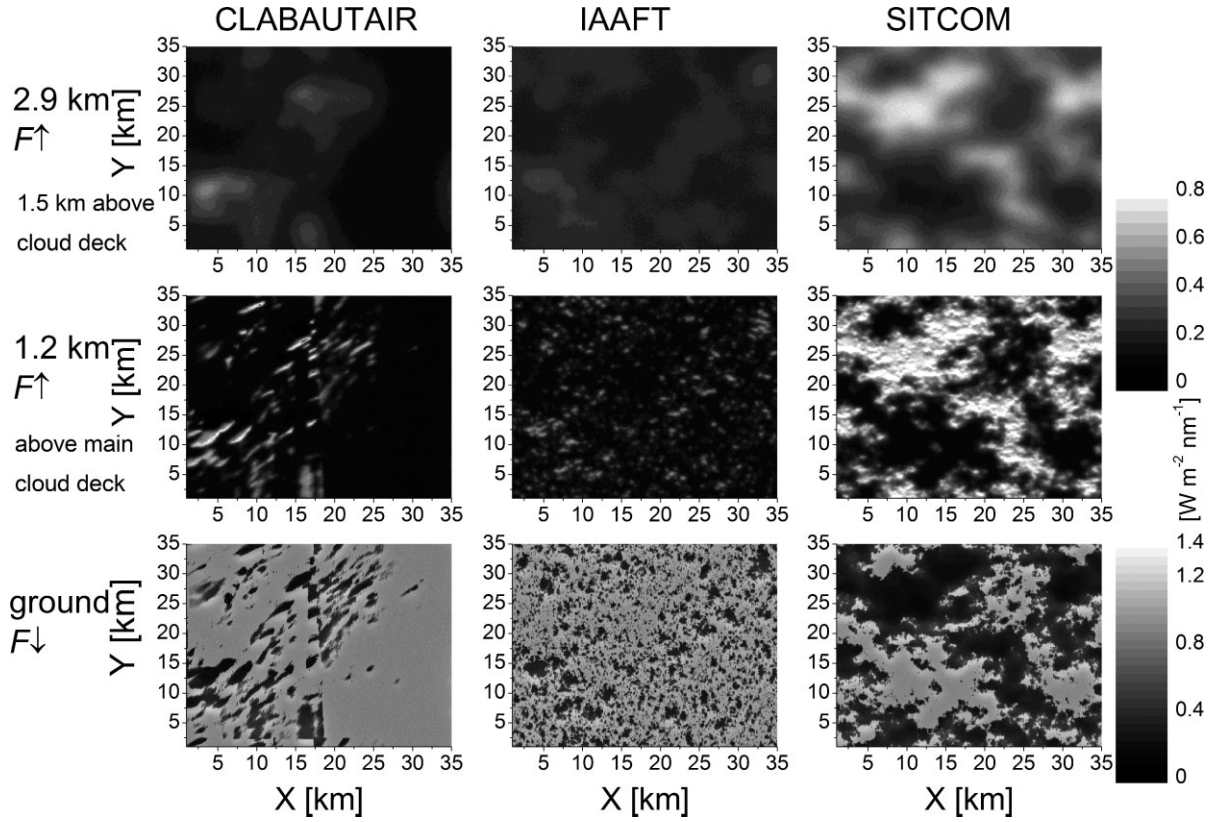

Figure 11. Horizontal distribution of simulated upward irradiance at 2.9 km and 1.2 km altitude, and downward irradiance at the ground (all at 500 nm), for the broken-cloud case.

ground and at 2.9 km altitude. The differences between the cloud generators are more obvious here than in the overcast case. For CLABAUTAIR, the clouds are mainly located in the vicinity of the original flight track, whereas for IAAFT and SITCOM, they are distributed over the whole model domain. Note that while the distribution at 2.9 km altitude is almost uniform for IAAFT and CLABAUTAIR, there is still some structure visible for SITCOM.

Figure 12 shows the simulated and measured power spectra of the downward irradiance at the ground. The modelled variance is much higher than in the overcast case. Unlike in the overcast case, the scaling of the variance is modelled correctly down to the smallest scales; this is in part due to the higher average cloud transmittance in the broken-cloud case, with more photons reaching the ground. SITCOM is in closest agreement with the measured power spectrum (grey line) at all scales. Again in contrast to the overcast case, the simulated and measured power spectra do not deviate from the $k^{-5/3}$ power law. The measured autocorrelation length of the 500 nm downward irradiance at 1.0 km altitude (where most clouds were located) (0.5 km) is almost correctly reproduced by IAAFT and CLABAUTAIR (0.4 km) and overestimated by SITCOM (1.3 km). Note that the autocorrelation length of the measured LWC (0.2 km) is *less* than that observed for the corresponding irradiance (0.5 km), in contrast to the overcast case.

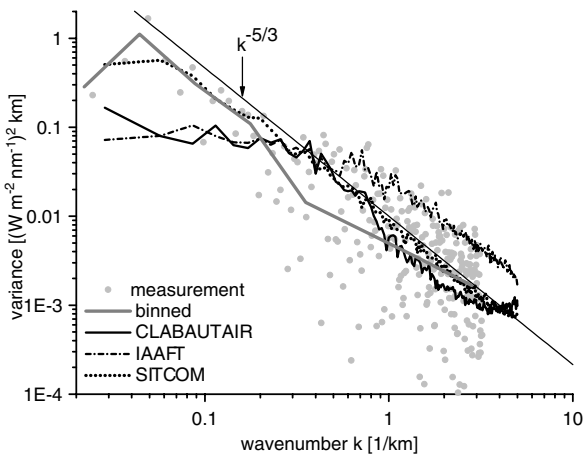

Figure 12. Power spectrum of $F^{\downarrow}$ on the ground, for the broken-cloud case. Measurements are shown by grey symbols and the grey line (logarithmically binned power spectrum); simulations are shown by black lines. For comparison, the $k^{-5/3}$ power law is also shown.

6. Summary and conclusions

For one overcast and one broken-cloud case from INSPECTRO, 3D clouds were produced with three cloud generators, using microphysical aircraft measurements. The 3D fields of LWC and R_{eff} were used as input to 3D radiative transfer calculations, and the irradiance fields corresponding to the microphysical input were calculated. The reconstructed microphysical properties and

DOI: 10.1002/qj

irradiance fields were then compared with the measurements.

6.1. Microphysical properties

In the analysis of the microphysical properties, we have considered the simulated and measured cloud-averaged LWC and its spatial variability quantified in terms of PDF and power spectra. Very encouragingly, for the overcast case, although the three generators use different approaches, only very small discrepancies are found in the reproduced microphysical parameters (LWC, LWP and R_{eff}). There is thus a small spread in the estimated optical thickness. For the broken-cloud case, the relative discrepancies are slightly larger, mostly because of disagreements in the reproduced cloud cover. Part of this problem comes through differences in the threshold values of LWC or drop size that are considered as cloud, which lead to significant differences if most of the cloud water is concentrated in small drops or in low-LWC domains. A possible discretization issue in CLABAUTAIR will be fixed in the next version.

The reproduced vertical profiles of LWC and R_{eff} for all three generators are in good agreement with the measurements in both cases. In particular, the distribution of LWC values within one representative height level is very well reproduced by CLABAUTAIR and IAAFT, while SITCOM generates a distribution with higher variability than measured. The greatest apparent differences between the generators occur in the LWP fields: the CLABAUTAIR fields show an accumulation of LWP for some locations, and the original flight track can be traced. This is because the measurements are directly mapped onto the model grid, whereas IAAFT and SITCOM generate fields that match the measurements in a statistical sense. Hence, while CLABAUTAIR is able to handle different cloud scenes and gradients within one grid, the quality of the reproduction decreases with increasing distance from actual data (i.e. from the flight track). IAAFT and SITCOM do not have this drawback, and their quality of reproduction does not depend on location or domain size. When the microphysical horizontal cloud variability is taken into account, it is found that the power spectra of the simulations are in fairly good agreement with the measurements, even though the structure of the LWP fields is remarkably different visually. In terms of autocorrelation length, only IAAFT reproduces the measurements for both cases.

6.2. Irradiance fields

For the overcast case, the measured and simulated profiles agree very well, as do the spectra of irradiance above and below the cloud layer. For IAAFT, the mean downward irradiance below the clouds and the mean upward irradiance above the clouds agrees with the measurements to within $12\,\mathrm{mW\,m^{-2}\,nm^{-1}}$. For the other two generators, the agreement is within $30\,\mathrm{mW\,m^{-2}\,nm^{-1}}$.

The irradiance calculations in the broken-cloud case are strongly influenced by the cloud cover. Nevertheless, the agreement between calculated and measured irradiance is within $20\,\mathrm{mW\,m^{-2}\,nm^{-1}}$ for IAAFT, $12\,\mathrm{mW\,m^{-2}\,nm^{-1}}$ for SITCOM, and $50\,\mathrm{mW\,m^{-2}\,nm^{-1}}$ for CLABAUTAIR. Details of the horizontal distribution of irradiance are revealed by the histograms of modelled and measured irradiance above and below the cloud level.

For the overcast case, the widths of the simulated and measured irradiance histograms compare well for CLABAUTAIR and IAAFT. SITCOM results show a higher variability than measured, for both the overcast and the broken-cloud cases. For the broken-cloud case, three modes are identified in the histograms for the ground-based histograms: the 'clear' peak, where radiation has not interacted with clouds; the 'cloudy' peak, where the direct beam is masked by the cloud and only the portion determined by cloud transmittance is measured; and the 'cloud edge' peak. This is a 3D effect in which the direct sun is not masked and the surrounding clouds enhance the measured irradiance by scattering light off the direct beam into the cloud-free area. This effect is best reproduced by IAAFT clouds, and is not seen in the IPA calculations, as expected. The relative heights of these three peaks change as the cloud cover varies. However, the positions of the individual modes do not change as the cloud cover varies. For reflected irradiance, the best agreement with the measurements is again achieved by IAAFT reproductions. For an additional IAAFT cloud reproduction, the cloud clover is forced to the value observed by MODIS for the given period and area. However, the modelling results can only be reconciled with the irradiance measurements by also using the satellite retrievals of effective drop radius, which are about three times as large as values measured *in situ*. If we trust the *in situ* measurements of the effective radius more than the satellite retrievals, then in this case we must conclude that the satellite-measured cloud cover is incorrect. However, no definitive statement can be made, because the time offset between the satellite retrieval and the microphysical measurements is too large.

As far as horizontal structure is concerned, the power spectra of the reproduced fields are in fairly good agreement with the measurements. For the overcast case, the number of photons is not sufficient to trace the scaling behaviour of the measured irradiance down to the smallest scales. However, the change from a $-5/3$ power law to a steeper descent is correctly reproduced by all three models at about 3 km. The position of this scale break changes according to the distance from the cloud. With IPA simulations, the $-5/3$ scaling is maintained at all scales, and no scale break is reproduced.

No wavelength-dependent 3D effect was found in the non-absorbing wavelengths. For the 936 nm wavelength, no statement can be made because of water vapour absorption. More work will be required to draw conclusions about full-spectrum or broadband irradiance.

DOI: 10.1002/qj

6.3. When are 3D simulations required?

6.3.1. One-point statistics

For the two cases examined in this study, we found that as far as domain-averaged irradiance is concerned, IPA results did not differ significantly from the 3D MC simulations and the measurements. For the broken-cloud case, the mean value is largely influenced by cloud cover, and horizontal photon transport is only of secondary importance. Unfortunately, cloud cover is a poorly defined parameter, both because of its 'fuzzy' definition and because of the methods of observation. Even if it is not known exactly, modelled and simulated irradiance fields can still be compared by looking at histograms of upward and downward irradiance above and below the cloud layer. To obtain the measured 'cloud edge' peak, IPA is *not* sufficient, even if we are only interested in one-point statistics.

Our model calculations were only performed for the solar zenith angles where radiation measurements were available. For overcast clouds, Di Giuseppe and Tompkins (2003) have calculated domain-averaged irradiance for a range of SZA and found no significant differences between IPA and 3D simulations. For broken clouds, Benner and Evans (2001) found no significant impact from horizontal photon transport for remotely-sensed clouds. Di Giuseppe and Tompkins (2003) report a good agreement between IPA and 3D only when the cloud horizontal variability is organized on scales above 10 km.

6.3.2. Two-point statistics

In order to reproduce the horizontal structure – in particular the irradiance scale break – correctly, 3D simulations are necessary. In the overcast case, IPA fails to reproduce the variance decrease of the measured irradiance field at scales below 10 km. This may be related to the aforementioned result of Di Giuseppe and Tompkins (2003) regarding the IPA bias in broken clouds. Above this scale, the $k^{-5/3}$ power law is correctly reproduced by both IPA and 3D simulation. However, the position of the scale break moves to higher scales as the distance from cloud top increases, because of geometrical smoothing. This means that at the top of the atmosphere the irradiance power spectra may be significantly steeper than those modelled by IPA over a range spanning hundreds of kilometres.

References

Anderson GP, Clough SA, Kneizys FX, Chetwynd JH, Shettle EP. 1986. *Atmospheric Constituent Profiles (0–120* km*)*. Hanscom AFB.

Benner TC, Evans KF. 2001. Three-dimensional solar radiative transfer in small tropical cumulus fields derived from high-resolution imagery. *J. Geophys. Res.* **106 (D14)**: 14975–14984.

Bowker DE, Davis RE, Myrik DL, Stacy K, Jones WT. 1985. *Spectral Reflectance of Natural Targets for Use in Remote Sensing Studies.* NASA Reference Publ. No. 1139.

Brenguier JL, Bourrianne T, Coelho AD, Isbert J, Peytavi R, Trevarin D, Weschler P. 1998. Improvements of droplet size distribution measurements with the Fast-FSSP (Forward Scattering Spectrometer Probe). *J. Atmos. Oceanic Technol.* **15**: 1077–1090.

Cahalan RF, Ridgway W, Wiscombe WJ, Bell TL, Snider JB. 1994. The albedo of fractal stratocumulus clouds. *J. Atmos. Sci.* **51**: 2434–2455.

Davies R. 1978. Effect of finite geometry on 3-dimensional transfer of solar irradiance in clouds. *J. Atmos. Sci.* **35**: 1712–1725.

Davis A, Marshak A, Cahalan R, Wiscombe W. 1997. The LANDSAT scale break in stratocumulus as a three-dimensional radiative transfer effect: Implications for cloud remote sensing. *J. Atmos. Sci.* **54**: 241–260.

Di Giuseppe F, Tompkins AM. 2003. Effect of spatial organization on solar radiative transfer in three-dimensional idealized stratocumulus cloud fields. *J. Atmos. Sci.* **60**: 1774–1794.

Evans KF, Lawson RP, Zmarzly P, O'Connor D, Wiscombe WJ. 2003. In situ cloud sensing with multiple scattering lidar: Simulations and demonstration. *J. Atmos. Oceanic Technol.* **20**: 1505–1522.

Evans KF, Wiscombe WJ. 2004. An algorithm for generating stochastic cloud fields from radar profile statistics. *Atmos. Res.* **72**: 263–289.

Gerber H, Ahrends BG, Ackerman AS. 1994. New microphysics sensor for aircraft use. *Atmos. Res.* **31**: 235–252.

Gobbi GP, Barnaba F, Ammannato L. 2004. The vertical distribution of aerosols, Saharan dust and cirrus clouds in Rome (Italy) in the year 2001. *Atmos. Chem. Phys.* **4**: 351–359.

Kite A. 1987. The albedo of broken cloud fields. *Q. J. R. Meteorol. Soc.* **113**: 517–531.

Kurucz RL. 1992. 'Synthetic infrared spectra in infrared solar physics', in *IAU Symp. 154*, Rabin DM and Jefferies JT (eds). Kluwer: Norwell, MA.

Kylling A, Webb AR, Kift R, Gobbi GP, Ammannato L, Barnaba F, Bais A, Kazadzis S, Wendisch M, Jäkel E, Schmidt S, Kniffka A, Thiel S, Junkermann W, Blumthaler M, Silbernagl R, Schallart B, Schmitt R, Kjeldstad B, Thorseth TM, Scheirer R, Mayer B. 2005. Spectral actinic flux in the lower troposphere: measurement and 1-D simulations for cloudless, broken cloud and overcast situations. *Atmos. Chem. Phys.* **5**: 1975–1997.

Los A, Duynkerke PG. 2000. Microphysical and radiative properties of inhomogeneous stratocumulus: Observations and model simulations. *Q. J. R. Meteorol. Soc.* **126**: 3287–3307.

Lovejoy S, Schertzer D. 1986. Scale invariance, symmetries, fractals, and stochastic simulations of atmospheric phenomena. *Bull. Am. Meteorol. Soc.* **67**: 21–32.

Marshak A, Davis A, Wiscombe W, Cahalan R. 1998. Radiative effects of sub-mean free path liquid water variability observed in stratiform clouds. *J. Geophys. Res.* **103**: 19557–19567.

Mayer B. 1999. 'I3RC phase 1 results from the MYSTIC Monte Carlo model'. Proceedings of the I3RC workshop, Tucson, Arizona, USA.

Mayer B. 2000. 'I3RC phase 2 results from the MYSTIC Monte Carlo model', in *Proceedings of the I3RC Workshop*, Tucson, Arizona, USA.

Mayer B, Kylling A. 2005. The libRadtran software package for radiative transfer calculations – description and examples of use. *Atmos. Chem. Phys.* **5**: 1855–1877.

Moeng CH, Cotton WR, Bretherton C, Chlond A, Khairoutdinov M, Krueger S, Lewellen WS, MacVean MK, Pasquier JRM, Rand HA, Siebesma AP, Stevens B, Sykes RI. 1996. Simulation of a stratocumulus-topped planetary boundary layer: Intercomparison among different numerical codes. *Bull. Am. Meteorol. Soc.* **77**: 261–278.

Neggers RAJ, Duynkerke PG, Rodts SMA. 2003. Shallow cumulus convection: A validation of large-eddy simulation against aircraft and Landsat observations. *Q. J. R. Meteorol. Soc.* **129**: 2671–2696.

Räisänen P, Isaac GA, Barker HW, Gultepe, I. 2003. Solar radiative tranfer for stratiform clouds with horizontal variations in liquid-water path and droplet effective radius. *Q. J. R. Meteorol. Soc.* **129**: 2135–2149.

Scheirer R, Schmidt S. 2005. CLABAUTAIR: A new algorithm for retrieving three-dimensional cloud structure from airborne microphysical measurements. *Atmos. Chem. Phys.* **5**: 2333–2340.

Schmidt S. 2005. 'Influence of cloud inhomogeneities on solar spectral radiation', PhD thesis, Leipzig University.

Stephens GL. 1978. Radiation profiles in extended water clouds. 2.: Parameterization schemes. *J. Atmos. Sci.* **35**: 2123–2132.

Venema V, Meyer S, Garcia SG, Kniffka A, Simmer C, Crewell S, Löhnert U, Trautmann T, Macke A. 2006. Surrogate cloud fields generated with the iterative amplitude adapted Fourier transform algorithm. *Tellus* **58B**(:): 104–120.

DOI: 10.1002/qj

Welch RM, Wielicki BA. 1984. Stratocumulus cloud field reflected fluxes – the effect of cloud shape. *J. Atmos. Sci.* **41**: 3085–3103.
Wendisch M, Garrett TJ, Strapp JW. 2002. Wind tunnel tests of the airborne PVM-100A response to large droplets. *J. Atmos. Oceanic Technol.* **19**: 1577–1584.
Wendisch M, Müller D, Schell D. 2001. An airborne spectral albedometer with active horizontal stabilization. *J. Atmos. Oceanic Technol.* **18**: 1856–1866.
Wiscombe WJ. 1980. Improved scattering algorithms. *Appl. Opt.* **19**: 1505–1509.

DOI: 10.1002/qj